The Effect of Magnetic Variability on Stellar Angular Momentum Loss. II. The Sun, 61 Cygni A, ϵ Eridani, ξ Bootis A, and τ Bootis A

Adam J. Finley [ORCID], Victor See, and Sean P. Matt [ORCID]
University of Exeter, Exeter, Devon, EX4 4QL, UK; *af472@exeter.ac.uk
Received 2019 January 14; revised 2019 March 22; accepted 2019 March 23; published 2019 May 1

Abstract

The magnetic fields of low-mass stars are observed to be variable on decadal timescales, ranging in behavior from cyclic to stochastic. The changing strength and geometry of the magnetic field should modify the efficiency of angular momentum loss by stellar winds, but this has not been well quantified. In Finley et al. (2018), we investigated the variability of the Sun and calculated the time-varying angular momentum-loss rate in the solar wind. In this work, we focus on four low-mass stars that have all had their surface magnetic fields mapped for multiple epochs. Using mass-loss rates determined from astrospheric Lyα absorption, in conjunction with scaling relations from the MHD simulations of Finley & Matt (2018), we calculate the torque applied to each star by their magnetized stellar winds. The variability of the braking torque can be significant. For example, the largest torque for ϵ Eri is twice its decadal averaged value. This variation is comparable to that observed in the solar wind, when sparsely sampled. On average, the torques in our sample range from 0.5 to 1.5 times their average value. We compare these results to the torques of Matt et al. (2015), who use observed stellar rotation rates to infer the long-time-averaged torque on stars. We find that our stellar wind torques are systematically lower than the long-time-averaged values, by a factor of ∼3–30. Stellar wind variability appears unable to resolve this discrepancy, implying that there remain some problems with observed wind parameters, stellar wind models, or the long-term evolution models, which have yet to be understood.

Key words: evolution – magnetohydrodynamics (MHD) – stars: low-mass – stars: winds, outflows – stars: magnetic field – stars: rotation

1. Introduction

For low-mass stars like the Sun ($M_* \lesssim 1.3\,M_\odot$), magnetic activity is observed to decline with stellar age (Hartmann & Noyes 1987; Mamajek & Hillenbrand 2008). This is a consequence of the dynamo mechanism, which is responsible for sustaining the stellar magnetic field, and its dependence on rotation and convection (Brun & Browning 2017). During the main sequence, angular momentum is removed by magnetized stellar winds. This wind braking increases the observed rotation periods of stars with age (Skumanich 1972; Bouvier et al. 2014). The connections between stellar rotation, magnetic activity, and wind braking converge the rotation and activity indices of low-mass stars during the main sequence, such that these quantities appear to follow a mass-dependent relationship with age (Noyes et al. 1984; Gilliland 1986; Wolff & Simon 1997; Stelzer & Neuhäuser 2001; Pizzolato et al. 2003; Barnes 2010; Meibom et al. 2015). This connection with age is useful in a number of ways. For example, empirical relations can be derived in order to determine the ages of some stars from their rotation or magnetic activity (Barnes 2003; Mamajek & Hillenbrand 2008; Meibom et al. 2009; Delorme et al. 2011; Van Saders & Pinsonneault 2013; Vidotto et al. 2014).

The observed evolution of rotation also provides a constraint on the torque applied to stars, independent of our understanding of stellar winds. Models for computing the rotational evolution of stars give us an indication of how stellar wind torques evolve on secular (up to several gigayear) timescales (e.g., Gallet & Bouvier 2013, 2015). These torques can then be compared to calculations that are based on observed wind and magnetic properties, in order to test our understanding of stellar magnetism and winds (Amard et al. 2016; Réville et al. 2016). One caveat, however, is that the torques derived from rotational evolution

models are only sensitive to the angular momentum losses of stars averaged over some fraction of the spin-down timescale. For Sun-like main sequence stars, the rotational evolution torques thus represent a value averaged over ∼10–100 Myr. Clearly, any variability of wind and magnetic properties on timescales shorter than this will inhibit a comparison between the long-time torque from rotational evolution models and those calculated based on observed present-day magnetic and wind properties.

Variability in the magnetic activity of low-mass stars is commonly observed at short timescales, ranging from days to years (Baliunas et al. 1995; Hall et al. 2007; Egeland et al. 2017). The magnetic fields are driven by the stellar dynamo, whose variability can take many forms—be it in exhibiting a cyclic magnetic field like that of the Sun (Boro Saikia et al. 2016; Jeffers et al. 2018), magnetic fields with multiple cycles (Jeffers et al. 2014), or magnetism with apparently stochastic behaviors (Petit et al. 2009; Morgenthaler et al. 2012). Such variability appears to occur throughout the main sequence lifetime of low-mass stars. It is therefore interesting to characterize the impact this has on the stellar wind torques.

In order to quantify the impact of magnetic variability on stellar wind braking, we first studied the solar wind in Finley et al. (2018, hereafter Paper I), for which we have both in situ observations of the wind plasma and remote observations of the photospheric magnetic field. In Paper I, available data allowed us to study the variability on timescales from one solar rotation (∼27 days) up to a few decades. We quantified how the torque varies on all timescales, and found that the decadal-averaged value was smaller than the rotational evolution torque by a factor of ∼15. Although the reason for the discrepancy is still not clear, it could be due to gaps in our understanding of the solar magnetism and wind, variability in the solar torque on

timescales much longer than a decade, issues with the rotational-evolution torques, or a combination thereof.

In the present paper, we examine the influence of observed magnetic variability on the wind braking of four Sun-like stars, using semi-analytic relations derived from MHD wind simulations, and we compare these values to the long-time-averaged torques derived from modeling the rotational evolution of low-mass stars. In Section 2, we first describe the semi-analytic wind braking formula from Finley & Matt (2017, 2018, hereafter FM18), and the rotational evolution torque prescription from Matt et al. (2015, hereafter M15). In Section 3, we gather stellar properties and magnetic field observations for our four sample stars: 61 Cyg A, ϵ Eri, ξ Boo A, and τ Boo A. Each star has repeat observations using the Zeeman–Doppler imaging (ZDI) technique, and three of them also have observed mass-loss rates estimated from astrospheric Lyα absorption. We also re-examine the Sun, limiting the available data to observations ∼2 yr apart, which is more comparable to the cadence of observations for the other stars. In Section 4, we calculate the angular momentum-loss rates using both torque formulas. We discuss our results in Section 5.

2. Angular Momentum-loss Prescriptions

2.1. Stellar Wind Torques from Finley & Matt (2018)

As in Paper I, we will make use of the semi-analytic formula derived from the MHD simulations of FM18. Such formulations are intended to characterize the braking torques on stars that host convective outer envelopes. In Paper I, we used a formulation based on the open magnetic flux in the solar wind. Such formulae are independent of the magnetic geometry at the stellar surface (Réville et al. 2015), but the open magnetic flux cannot be measured for stars other than the Sun. For this work, we instead use a formula based on the observed surface magnetic field. Previous formulae of this kind have only been valid for single magnetic geometries (Matt & Pudritz 2008; Matt et al. 2012; Réville et al. 2015; Pantolmos & Matt 2017), but the magnetic fields of low-mass stars are observed to contain mixed magnetic geometries that vary from star to star (e.g., See et al. 2016), as well as in time, with geometries evolving in strength with respect to one another (e.g., DeRosa et al. 2012, for the Sun).

The FM18 formulation is simplified, but is capable of approximating the observed behavior of full MHD simulations without the computational expense. The MHD simulations are performed using axisymmetric magnetic geometries combined with polytropic Parker-like wind solutions (Parker 1958; Pneuman & Kopp 1971; Keppens & Goedbloed 1999), which are relaxed to a steady state. The application of results derived from such simulations to a time-varying problem emulates a sequence of independent steady-state solutions. Given that the characteristic timescales for disturbances caused by the reorganization of the coronal magnetic field to propagate through the solution are short with respect to the evolution of the system, this is a valid approximation.

The torque due to a stellar wind is prescribed in terms of the average Alfvén radius, $\langle R_A \rangle$, which acts as an efficiency factor for the stellar wind in extracting angular momentum (Weber & Davis 1967; Mestel 1968). The torque, τ, is given by

$$\tau = \dot{M}\Omega_* R_*^2 \left(\frac{\langle R_A \rangle}{R_*}\right)^2, \qquad (1)$$

where $\dot{M}$ is the mass-loss rate of the stellar wind, Ω_* is the stellar rotation rate (approximated as solid body rotation at the surface), and R_* is the stellar radius. In FM18, $\langle R_A \rangle$ is parameterized in terms of the wind magnetization,

$$\Upsilon = \frac{B_*^2 R_*^2}{\dot{M} v_{\rm esc}}, \qquad (2)$$

where the total field strength is evaluated from the first three spherical harmonic components $B_* = |B_{\rm dip}| + |B_{\rm quad}| + |B_{\rm oct}|$, the escape velocity is given by $v_{\rm esc} = \sqrt{2GM_*/R_*}$, and M_* is the stellar mass. Previous works have shown the reduced efficiency of magnetic braking with increasingly complex magnetic fields (Réville et al. 2015; Garraffo et al. 2016). Furthermore, FM18 examined the behavior of mixed magnetic geometries. They were able to show that higher-order modes (e.g., octupole) play a diminishing role in braking stellar rotation, when modeled in conjunction with lower-order modes (e.g., dipole, quadrupole). For mixed geometries, FM18 showed that the average simulated Alfvén radius behaves approximately as a broken power law of the form

$$\frac{\langle R_A \rangle}{R_*} = \max \begin{cases} K_{\rm dip}[\mathcal{R}_{\rm dip}^2 \Upsilon]^{m_{\rm dip}}, \\ K_{\rm quad}[(\mathcal{R}_{\rm dip} + \mathcal{R}_{\rm quad})^2 \Upsilon]^{m_{\rm quad}}, \\ K_{\rm oct}[(\mathcal{R}_{\rm dip} + \mathcal{R}_{\rm quad} + \mathcal{R}_{\rm oct})^2 \Upsilon]^{m_{\rm oct}}. \end{cases} \qquad (3)$$

This approximates the stellar wind solutions from Finley & Matt (2018), for their fit parameters $K_{\rm dip} = 1.53$, $K_{\rm quad} = 1.70$, $K_{\rm oct} = 1.80$, $m_{\rm dip} = 0.229$, $m_{\rm quad} = 0.134$, and $m_{\rm oct} = 0.087$. The magnetic field geometry is input using $\mathcal{R}_{\rm dip}$, $\mathcal{R}_{\rm quad}$, and $\mathcal{R}_{\rm oct}$, defined as the ratios of the polar strengths for each component over the total field strength, i.e., $\mathcal{R}_{\rm dip} = |B_{\rm dip}|/B_*$, etc. We neglect modes of higher order than the octupole, as they do not significantly contribute to the torque on the star.

2.2. Rotation Evolution Torques from Matt et al. (2015)

In this work, we will compare our results to the rotation evolution model of M15, which uses the observed distribution of mass versus rotation, at given ages, to find empirical torques that reproduce these observations. To date, no single model (including M15) precisely reproduces the observed mass-rotation distributions, but M15 reproduces the broad dependences of rotation rates on mass and age. The torque in this model has two regimes: either unsaturated, where the stellar Rossby number (defined as $Ro = 2\pi/(\Omega_* t_{\rm cz})$, where $t_{\rm cz}$ is the convective turnover time) is greater than the saturation value, $Ro_{\rm sat} = 0.1 Ro_{\odot}$; or saturated, where the Rossby number is smaller. All the stars in this paper are in the unsaturated regime. The M15 torque is given by

$$\tau = \tau_0 \left(\frac{t_{\rm cz}}{t_{\rm cz\odot}}\right)^p \left(\frac{\Omega_*}{\Omega_\odot}\right)^{p+1} \qquad (Ro_* > Ro_{\rm sat}), \qquad (4)$$

$$\tau = \tau_0 (10)^p \left(\frac{\Omega_*}{\Omega_\odot}\right) \qquad (Ro_* \leqslant Ro_{\rm sat}), \qquad (5)$$

where p is constrained by observations to ∼2 (Skumanich 1972), and τ_0 provides the normalization to the torque based on

Table 1
Stellar Parameters

Star Name	Mass ($M_\odot$)	Radius ($R_\odot$)	Teff (K)	t_{cz} (days)	Rot. Period (days)	Rossby Number	Cyc. Period (yr)	$\dot{M}$ ($\dot{M}_\odot$)
Sun	1.00	1.00	5780	12.7	28	2.20	11	1
61 Cyg A	0.66	0.67	4310	34.5	35.5	1.03	7.3	0.5
ϵ Eri	0.86	0.74	4990	24.0	11.7	0.49	3.0	30
ξ Boo A	0.93	0.86	5410	18.3	6.4	0.35	7.5[a]	5
τ Boo A	1.34	1.42	6460	1.88	3.0	1.60	0.3	$\sim$150[b]

Notes.
[a] Fit from this work.
[b] Average mass-loss rate from the MHD simulations of Nicholson et al. (2016).

the stellar mass and radius,

$$\tau_0 = 6.3 \times 10^{30} \mathrm{erg} \left(\frac{R_*}{R_\odot}\right)^{3.1} \left(\frac{M_*}{M_\odot}\right)^{0.5}, \quad (6)$$

which is fit empirically from the observed rotation rates of Sun-like stars.

For determining the convective turnover timescales, as in M15, we adopt the fit of Cranmer & Saar (2011) to the stellar models of Gunn et al. (1998),

$$t_{cz} = 314.24 \exp\left[-\left(\frac{T_{\mathrm{eff}}}{1952.5 \ \mathrm{K}}\right) - \left(\frac{T_{\mathrm{eff}}}{6250 \ \mathrm{K}}\right)^{18}\right] + 0.002, \quad (7)$$

where the effective temperature, T_{eff}, is the only variable determining t_{cz}. Cranmer & Saar (2011) showed this to be a reasonable approximation that is valid for the temperature range $3300 \leqslant T_{\mathrm{eff}} \leqslant 7000$ K. Such a monotonic function of $t_{cz}(T_{\mathrm{eff}})$ is also supported by other works (Barnes & Kim 2010; Landin et al. 2010).

3. Observed Stellar Properties

We select a sample from all stars that have been monitored with ZDI, requiring that each have six or more ZDI observations that clearly show magnetic variability. This criterion selects four stars, as most stars that have been observed with ZDI have only one or two epochs. Along with our sample stars, we also consider the Sun. This section contains information on each star, including results from ZDI, studies of their astrospheric Lyα absorption, and proxies of their magnetic activity. Both solar and stellar parameters can be found in Table 1.
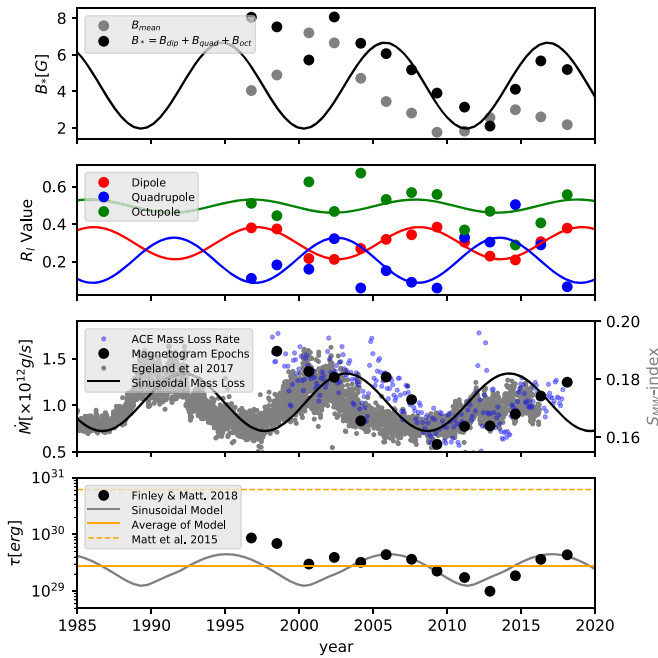
3.1. The Sun

The study of the Sun's magnetism has afforded the astrophysics community a great wealth of information on the apparent behavior of the magnetic dynamo process (Brun et al. 2015). We observe the Sun to have a cyclic pattern in its magnetic activity, with a sunspot cycle of around 11 yr and a magnetic cycle lasting approximately 22 yr (Babcock 1961; Schrijver & Liu 2008; DeRosa et al. 2012). At the minimum of magnetic activity, the wind dynamics on large scales are dominated by the axisymmetric dipole component and the solar wind is, in general, fast and diffuse, emerging on open polar field lines (Wang & Sheeley 1990; Schwenn 2006). As the cycle progresses, the solar magnetic field becomes increasingly complex toward maximum, with the appearance of sunspots as buoyant magnetic flux tubes rise through the photosphere (Parker 1955; Spruit 1981; Caligari et al. 1995; Fan 2008). Due to the increased complexity, more of the solar wind emerges in the slow, dense component, and transient magnetic phenomena are more frequent (Webb & Howard 1994; Neugebauer et al. 2002; McComas et al. 2003). The average surface magnetic field is stronger at maximum, and so too are magnetic activity indicators and the solar irradiance (Lean et al. 1998; Wenzler et al. 2006). Following the decline of magnetic activity into the next minimum, the polarity of the field is reversed (Babcock 1959; Sun et al. 2015). Numerous mechanisms have been proposed to explain this phenomenon (e.g., Fisher et al. 2000; Ossendrijver 2003). The solar magnetic field returns to its original polarity after one further sunspot cycle, completing the magnetic cycle.

As was done for the Sun in Paper I, we use synoptic magnetograms taken by the Michelson Doppler Imager on board the *Solar and Heliospheric Observatory* (*SOHO*/MDI) and the Helioseismic and Magnetic Imager on board the *Solar Dynamic Observatory* (*SDO*/HMI). We calculate the average surface magnetic field strength B_{mean}, the combined polar dipole, quadrupole and octupole field strength B_*, and the field fractions $\mathcal{R}_{\mathrm{dip}}$, $\mathcal{R}_{\mathrm{quad}}$, and $\mathcal{R}_{\mathrm{oct}}$. Unlike Paper I, in order to better compare the solar case with other stars, and to illustrate the effect of sparse time sampling, we take only 13 Carrington rotations, equally spaced over the $\sim$20 yr of data. This information is plotted in the top two panels of Figure 1 and tabulated in Appendix A.

The first panel of Figure 1 compares the average surface magnetic field, B_{mean}, which is often used when discussing results from ZDI, to the combined polar field strength of the lowest three spherical harmonic components, B_*, which is required by the FM18 torque formulation. Typically, B_* is larger than B_{mean}, because it sums the absolute magnitude of the polar field strengths, whereas B_{mean} allows for opposing field polarities to cancel and is averaged over the stellar surface.

Sparsely sampling the solar magnetograms has made the well-known cyclic behavior of the large-scale magnetic field less obvious, especially when considering B_*. However, the cycle is more clear in the second panel, where we plot the fraction of B_* in the dipole, quadrupole, and octupole components. We illustratively recover the magnetic behavior of the Sun by fitting sinusoids of B_*, $\mathcal{R}_{\mathrm{dip}}$, $\mathcal{R}_{\mathrm{quad}}$, and $\mathcal{R}_{\mathrm{oct}}$ with a fixed 11 yr period, and allowing the phase and amplitude of each fit to vary. These illustrations are shown in Figure 1, and will be repeated for the ZDI sample in Section 3.3 to produce feasible distributions of magnetic properties for each star,

Figure 1. Angular momentum-loss calculation for the solar wind (the Sun-as-a-star approach). The top two panels show the magnetic field properties of the Sun using synoptic magnetograms from *SOHO*/MDI and *SDO*/HMI. Dots represent sparsely sampled epochs of observation. The first panel shows the evolution of the magnetic field strength at the surface of the Sun. The second panel shows the ratio of dipole, quadrupole, and octupole components to the combined (dipole, quadrupole, and octupole) magnetic field strength. The third panel displays the mass-loss rate measurements derived from the *ACE* spacecraft (see Paper I) in blue, with the the selected epochs shown with black dots (left scale), along with the evolution of solar *S*-index from Egeland et al. (2017) indicated by gray dots (right scale). We fit sinusoids to the magnetic and mass-loss rate variables with a fixed 11 yr period, which roughly represents the solar chromospheric activity cycle. Black dots in the fourth panel indicate the calculated torques for each magnetogram epoch using FM18. The torque using our continuous sinusoidal fits is plotted as a solid gray line, and its average is highlighted by a solid orange horizontal line. The torque calculated using M15 is indicated by a dashed orange horizontal line.

allowing us to further examine the role of magnetic variability on stellar wind torques.

3.2. Other Stars

Four stars observed with ZDI meet our criteria for selection: 61 Cyg A, ϵ Eri, ξ Boo A, and τ Boo A. Their basic properties are compiled in Table 1. Masses are determined using the stellar evolution model of Takeda et al. (2007). If available, radii are evaluated with interferometry by Kervella et al. (2008), Baines & Armstrong (2011), or Boyajian et al. (2013); otherwise, they are evaluated spectroscopically by Borsa et al. (2015). Effective temperatures are taken from Boeche & Grebel (2016), and then used in conjunction with Equation (7) to produce convective turnover timescales. Rotation periods for each star are determined by Boro Saikia et al. (2016), Rüedi et al. (1997), Toner & Gray (1988), Donahue et al. (1996), Donati et al. (2008), and Fares et al. (2009), respectively. These are then used to calculate the Rossby number $R_o = P_{rot}/t_{cz}$ for each object. Further details for each star are listed below.

61 Cyg A (HD 201091) is a K5V star, located 3.5 pc away (Brown et al. 2016) in the constellation of Cygnus as a visual binary with 61 Cyg B, a K7V star. Age estimations for 61 Cyg A range from 1.3 to 6.0 Gyr, with the majority of estimates at the younger end of this range: 2 Gyr (Barnes 2007), 3.6 Gyr

(Mamajek & Hillenbrand 2008), 6 Gyr (Kervella et al. 2008), and 1.3 Gyr (Marsden et al. 2014). Cyclic chromospheric/coronal activity is detected in many forms, including X-ray emission (Robrade et al. 2012), with a period in phase with its magnetic activity cycle (Baliunas et al. 1995; Boro Saikia et al. 2016, 2018).

ϵ Eri (HD 22049) is a K2V star in the constellation of Eridanus, at a distance of 3.2 pc (Brown et al. 2016). ϵ Eri is a young star with multiple age estimations (e.g., Song et al. 2000; Fuhrmann 2004). From gyrochronology, Barnes (2007) arrives at an age of 400 Myr, which is thought to be the most reliable (see discussion in Janson et al. (2008)). Chromospheric activity has been recorded for ϵ Eri by Metcalfe et al. (2013). It displays an activity cycle length of $\sim$3 yr, as well as a longer one of $\sim$13 yr that vanished after a 7 yr minimum in activity around 1995.

ξ Boo A (HD 131156A), a spectral-type G7V, lies in the constellation of Boötes, 6.7 pc away (Brown et al. 2016), in a visual binary with ξ Boo B of spectral type K5V. The age of ξ Boo A is determined from gyrochronology by Barnes (2007) as 200 Myr. Variations in ξ Boo A's chromospheric activity have been noted by multiple authors (Hartmann et al. 1979; Gray et al. 1996; Morgenthaler et al. 2012), but no clear cycle has been detected.

τ Boo A (HD 120136) is a very well-studied planet-hosting F7V star, sitting at a distance of 15.7 pc (Brown et al. 2016) in a multiple star system with τ Boo B, a faint M2V companion. τ Boo A has an age of around 1 Gyr (Borsa et al. 2015), and has an observed chromospheric activity cycle (Mengel et al. 2016; Mittag et al. 2017) that is in phase with the reversals of its global magnetic field (Jeffers et al. 2018). This is also the case for the Sun and 61 Cyg A. As τ Boo A has a close-in planetary companion, Walker et al. (2008) searched for star–planet interactions and found that the planet is likely inducing an active region on the stellar surface, causing further variability in the star's chromospheric emission.

3.3. Zeeman–Doppler Imaged Fields

61 Cyg A (Boro Saikia et al. 2016), ϵ Eri (Jeffers et al. 2014, 2017), ξ Boo A (Morgenthaler et al. 2012), and τ Boo A (Fares et al. 2009; Mengel et al. 2016; Jeffers et al. 2018) have all been monitored with ZDI. This is a tomographic technique that is capable of reconstructing their large-scale photospheric magnetic fields (Donati et al. 1989; Semel 1989; Brown et al. 1991; Donati & Brown 1997; Donati & Landstreet 2009). Magnetic fields cause spectral lines to split and become polarized due to the Zeeman effect (Zeeman 1897). By monitoring this splitting over multiple phases, taking advantage of the Doppler shifts due to rotation, and combining multiple line profiles together using a Least Squares Deconvolution (LSD) technique (Donati et al. 1997), the large-scale stellar magnetic field topology can be reconstructed.

Papers reporting ZDI results typically tabulate the fraction of the total magnetic field energy that is poloidal (E_{pol}) and the fraction of this poloidal field energy that is dipolar, quadrupolar, or octupolar (E_{dip}, E_{quad}, and E_{oct}), as well as the average surface field (B_{mean}). For the maps of Fares et al. (2009) and Mengel et al. (2016), we compute the values using data supplied by the authors; these values are not tabulated in the original papers. Using MHD stellar wind models, Jardine et al. (2013) were able to show that large-scale wind dynamics are largely unaffected by toroidal magnetic field structures
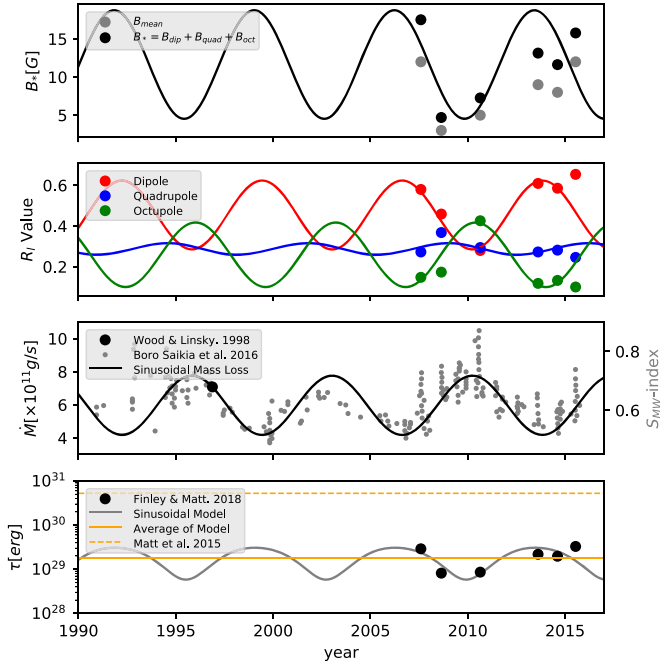
Figure 2. Angular momentum-loss calculation for 61 Cyg A. The top two panels show the magnetic field properties taken from the ZDI measurements of Boro Saikia et al. (2016). The first panel shows the evolution of the average unsigned magnetic field strength and the combined (dipole, quadrupole, and octupole) magnetic field strength, at the surface of the star. The second panel shows the ratios of dipole, quadrupole, and octupole components of the magnetic field to the combined magnetic field strength. We fit sinusoids to these properties with a fixed period of 7.3 yr, matching the chromospheric activity cycle. The third panel displays the mass-loss rate measurement of Wood & Linsky (1998) as a black dot, along with the S-index evolution of the chromospheric activity as gray dots (Boro Saikia et al. 2016). A sinusoidal mass-loss rate with a solar-like amplitude, as well as phase and period matching the observed chromospheric activity, is shown as a solid black line. Black dots in the fourth panel display the calculated torques for each ZDI epoch using FM18. A solid gray line plots the torque using our continuous sinusoidal fits; its average is highlighted by a solid orange horizontal line. The torque calculated using M15 is indicated with a dashed orange horizontal line.

embedded in the photosphere. Therefore, we assume the toroidal component does not impact our torque calculations. We convert the percentage energies into the poloidal dipole, quadrupole, and octupole field fractions, as well as combined field strength,

$$f_{\text{dip}} = \sqrt{E_{\text{pol}}E_{\text{dip}}}, \tag{8}$$

$$f_{\text{quad}} = \sqrt{E_{\text{pol}}E_{\text{quad}}}, \tag{9}$$

$$f_{\text{oct}} = \sqrt{E_{\text{pol}}E_{\text{oct}}}, \tag{10}$$

$$B_* = B_{mean}(f_{\text{dip}} + f_{\text{quad}} + f_{\text{oct}}). \tag{11}$$

Here, care has been taken in transforming fractional energy into fractional field strengths for each magnetic component. Subsequently, the field fractions, $f_{\text{dip}}, f_{\text{quad}}$, and f_{oct} are converted into the ratios of each magnetic component to the combined field strength, $\mathcal{R}_l$,

$$\mathcal{R}_{\text{dip}} = \frac{B_{\text{dip}}}{B_*} \equiv \frac{f_{\text{dip}}}{f_{\text{dip}} + f_{\text{quad}} + f_{\text{oct}}}, \tag{12}$$

$$\mathcal{R}_{\text{quad}} = \frac{B_{\text{quad}}}{B_*} \equiv \frac{f_{\text{quad}}}{f_{\text{dip}} + f_{\text{quad}} + f_{\text{oct}}}, \tag{13}$$
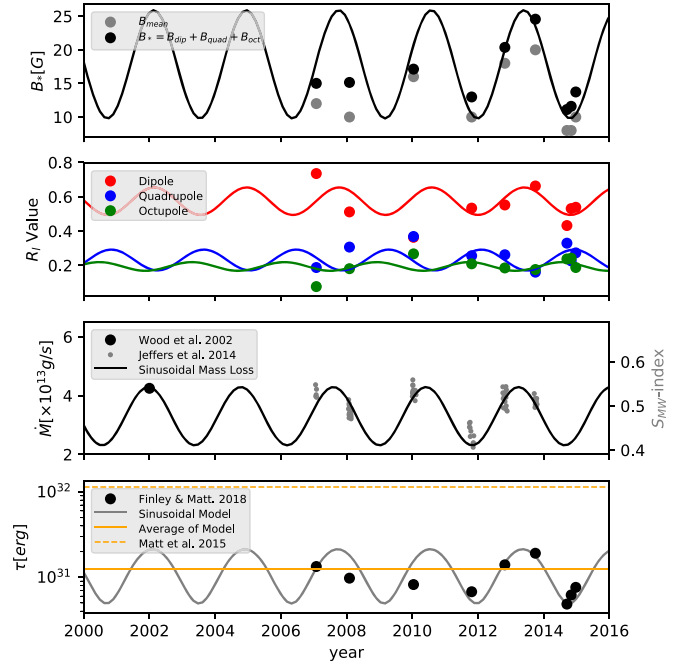
Figure 3. Same as Figure 2, but for ϵ Eri.

$$\mathcal{R}_{\text{oct}} = \frac{B_{\text{oct}}}{B_*} \equiv \frac{f_{\text{oct}}}{f_{\text{dip}} + f_{\text{quad}} + f_{\text{oct}}}. \tag{14}$$

These results are shown in the top two panels in each of Figures 2–5, and tabulated in Table 2 for each ZDI epoch. Calculating the ratios of each field component using this method, rather than recomputing the field strengths of each component from the original ZDI maps, introduces some errors that will be discussed in Section 5.1.

In each of Figures 2–5, the first panel displays the recorded mean magnetic field from the ZDI reconstructions, B_{mean}, with gray dots. The black dots represent the combined polar field strength of the dipole, quadrupole, and octupole components, B_*. Typically, the B_* value is larger than B_{mean}, unless a significant fraction of the magnetic energy is stored in the toroidal or high-order ($l > 3$) components. The second panels show the varying field fractions, $\mathcal{R}_{\text{dip}}$, $\mathcal{R}_{\text{quad}}$, and $\mathcal{R}_{\text{oct}}$.

Although multiple magnetic maps exist for each of our ZDI stars, they are still sampled relatively sparsely, compared to the Sun. To examine their variability further, we fit sinusoidal functions to B_*, $\mathcal{R}_{\text{dip}}$, $\mathcal{R}_{\text{quad}}$, and $\mathcal{R}_{\text{oct}}$, as we did for the Sun, using chromospheric activity periods taken from the literature for each star (see Table 1). We allow the phase and amplitude of each fit to vary, but we constrain the fits of $\mathcal{R}_{\text{dip}}$, $\mathcal{R}_{\text{quad}}$, and $\mathcal{R}_{\text{oct}}$ to sum to ∼1. In some cases, there is no strong evidence for periodicity—and even if so, a sinusoidal behavior is a gross simplification. We do this simply to illustratively construct continuous predictions for feasible cyclic behaviors, from which we can make more general comments about the impact of stellar cycles on stellar wind torques.

3.4. Inferred Mass-loss Rates and Activity Proxies

The solar mass-loss rate is observed to be variable in time (Hick & Jackson 1994; Webb & Howard 1994; McComas et al. 2000, 2013). In the third panel of Figure 1, we use blue dots to plot the solar mass-loss rate calculated in Paper I, based on data
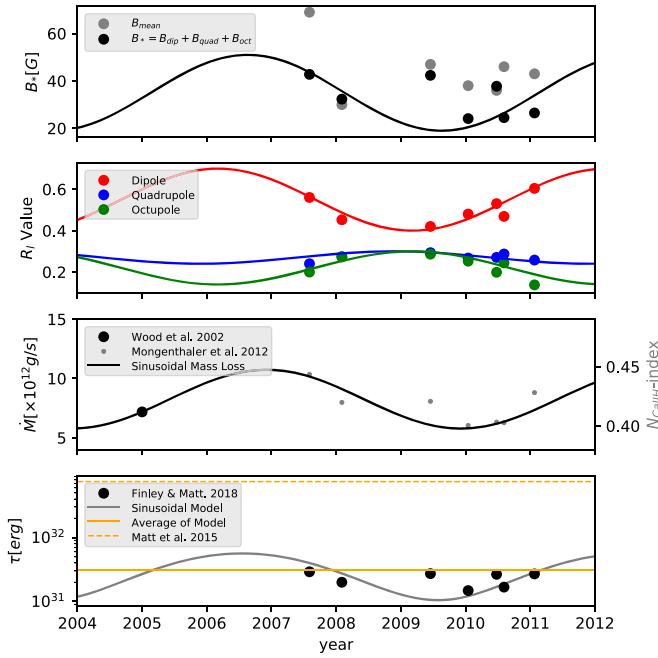
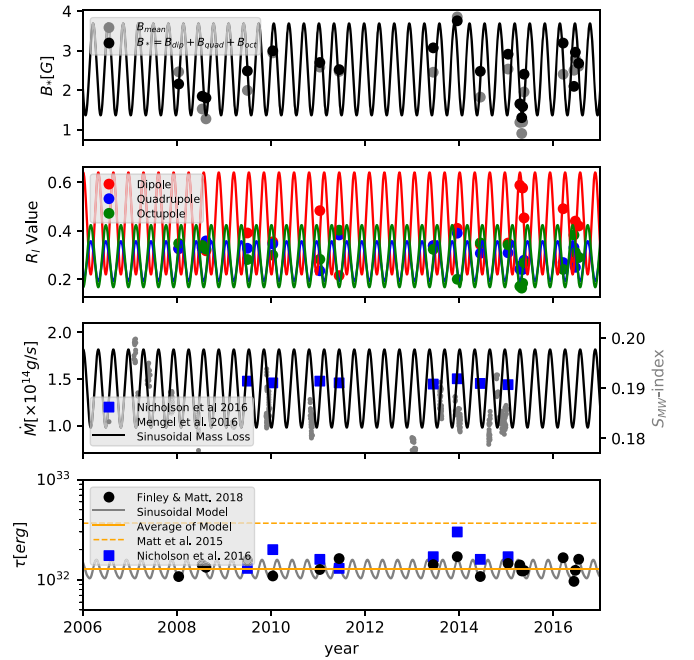**Figure 4.** Same as Figure 2, but for ξ Boo A.

Figure 5. Same as Figure 2, but for τ Boo A. Mass-loss rate and torque panels (3 and 4) include values (blue squares) from the MHD simulations of τ Boo A from Nicholson et al. (2016). A phase-folded version of this plot is available in Appendix B.

from the *Advanced Composition Explorer*[1], and we highlight our selected magnetogram epochs with black dots. During the solar cycle, the mass-loss rate from Paper I is found to vary around the mean by about ±30%.[2] We fit the function,

$$\dot{M}(t) = \langle \dot{M} \rangle \left[0.3 \sin\left(\frac{2\pi t}{P} + \phi \right) + 1 \right], \quad (15)$$

to the 13 selected magnetogram epochs. Here, t is the decimal year (1985–2020 are plotted), the mass-loss rate variation is constrained to $\Delta\dot{M} = 0.6\langle\dot{M}\rangle$, and the period is fixed as that of the chromospheric activity period, $P = 11$ yr. The fit values of the phase, ϕ, and the average mass-loss rate, $\langle\dot{M}\rangle$, are $\sim\pi/6$ and 1.03×10^{12} g s^{-1}, respectively. This fit is displayed as a solid black line in the third panel.

For nearby stars, Lyα observations can reveal information about their stellar winds (Wood 2004). Absorption in this line occurs at the edge of the star's astrosphere, as well as at the Sun's heliosphere. At these locations, the solar and stellar winds collide with the ISM and become shocked, reaching temperatures and densities much greater than the average ISM. Based on their models of this absorption, estimated mass-loss rates are available from Wood & Linsky (1998) and Wood et al. (2002, 2005) for 61 Cyg A, ϵ Eri, and ξ Boo A. There are no measurements of the mass-loss rate for τ Boo A, so instead we use the results of MHD simulations from Nicholson et al. (2016). The mass-loss rate used for each star is shown in Table 1.

For the ZDI stars, the mass-loss rates gathered from Lyα observations are taken at a single epoch. These are plotted as black dots in the third panel of Figures 2–4. However, we might expect the mass-loss rates of these stars to vary with their magnetic activity, similarly to the Sun. Currently, there are no observations in the literature capable of quantifying this variability, so we must draw comparisons with the Sun.

Increased emission in Ca II H&K is thought to correlate directly with the deposition of magnetic energy into the stellar chromosphere (Eberhard & Schwarzschild 1913; Noyes et al. 1984; Testa et al. 2015). This is observed for the Sun (Schrijver et al. 1989) and can be correlated with the mass-loss rate of the solar wind. Overplotted with the mass-loss rates in Figure 1, we show the solar S-index values from Egeland et al. (2017). The S-index evaluates the flux in the H and K lines and normalizes it to the nearby continuum (Wilson 1978). Both the solar mass-loss rate and the sinusoidal fit to our selected epochs appear roughly in phase with this measure of chromospheric activity. The slight lag between mass-loss rate and magnetic activity is not surprising, as a similar lag is observed in the rate of coronal mass ejections (Ramesh 2010; Webb & Howard 2012) and open magnetic flux in the solar wind (Wang et al. 2000; Owens et al. 2011). The Ca II H&K lines are now regularly monitored for hundreds of stars (Wilson 1978; Baliunas et al. 1995; Hall et al. 2007; Egeland et al. 2017). Using gray dots, we plot the available S-index measurements for each star in the third panel of Figures 2–5. The temporal coverage differs from star to star, with ξ Boo A having only the Ca II H band index,[3] taken concurrently with the ZDI observations (Morgenthaler et al. 2012).

Similarly to the Sun, we represent the mass-loss variation for each star using a sinusoidal function,

$$\dot{M}(t) = 0.3\langle\dot{M}\rangle\left[\sin\left(\frac{2\pi t}{P} + \phi \right) - \sin\left(\frac{2\pi t_{\mathrm{obs}}}{P} + \phi \right) \right] + \dot{M}_{\mathrm{obs}}, \quad (16)$$

with the phase, ϕ, and period, P, matching the variation of their Ca II H&K emission. We use chromospheric activity periods from

---

[1] http://srl.caltech.edu/ACE/ASC/level2/
[2] In calculating this variation, we ignore extreme values that are seen in time averages shorter than a few months.

---

[3] As both the H and K lines scale together, only information about one is required.

Table 2
Magnetic Properties from ZDI and Angular Momentum-loss Results

Star Name	ZDI Obs Epoch	B_* (G)	$\mathcal{R}_{dip}$ $\equiv B_{dip}/B_*$	$\mathcal{R}_{quad}$ $\equiv B_{quad}/B_*$	$\mathcal{R}_{oct}$ $\equiv B_{oct}/B_*$	$\langle R_A\rangle/R_*$	τ_{FM18} ($\times 10^{30}$ erg)	τ_{spinev} ($\times 10^{30}$ erg)	τ_{spinev} /$\langle\tau_{FM18}\rangle$	Reference (ZDI Data)
61 Cyg A	2007.59	17.5	0.58	0.27	0.15	11.8	0.29	5.25	26.25	1
	2008.64	4.7	0.46	0.37	0.17	5.5	0.08	...	...	1
	2010.55	7.3	0.28	0.29	0.43	5.1	0.09	...	...	1
	2013.61	13.1	0.61	0.27	0.12	10.9	0.22	...	...	1
	2014.61	11.6	0.59	0.28	0.13	9.9	0.20	...	...	1
	2015.54	15.6	0.65	0.25	0.10	11.4	0.32	...	...	1
ϵ Eri	2007.08	15.0	0.74	0.19	0.08	4.7	13.4	114	11.41	2
	2007.09	15.1	0.51	0.31	0.18	4.0	9.8	...	...	2
	2010.04	17.1	0.36	0.37	0.27	3.5	8.2	...	...	2
	2011.81	13.0	0.53	0.26	0.21	4.2	6.8	...	...	2
	2012.82	20.3	0.55	0.26	0.19	4.7	14.0	...	...	2
	2013.75	24.6	0.66	0.16	0.18	5.6	19.1	...	...	2
	2014.71	11.1	0.43	0.33	0.24	3.6	4.8	...	...	3
	2014.84	11.6	0.53	0.23	0.24	4.0	6.2	...	...	3
	2014.98	13.7	0.54	0.27	0.19	4.2	7.6	...	...	3
ξ Boo A	2007.56	42.8	0.56	0.24	0.20	11.0	29.1	748	32.4	4
	2008.09	32.3	0.45	0.27	0.27	8.5	20.0	...	...	4
	2009.46	42.4	0.42	0.29	0.29	8.8	27.3	...	...	4
	2010.04	24.1	0.48	0.27	0.25	7.9	14.8	...	...	4
	2010.48	37.8	0.53	0.27	0.20	9.8	26.6	...	...	4
	2010.59	24.5	0.47	0.29	0.24	7.4	16.8	...	...	4
	2011.07	26.5	0.60	0.26	0.14	8.1	27.0	...	...	4
τ Boo A	2008.04	2.2	0.33	0.33	0.35	2.1	108	367	2.72	5
	2008.54	1.8	0.33	0.33	0.34	2.0	141	...	...	5
	2008.62	1.8	0.32	0.36	0.32	2.0	133	...	...	5
	2009.5	2.5	0.39	0.33	0.28	2.1	156	...	...	5
	2010.04	3.0	0.35	0.35	0.30	2.2	109	...	...	6
	2011.04	2.7	0.48	0.23	0.28	2.1	127	...	...	6
	2011.45	2.5	0.22	0.38	0.40	2.1	163	...	...	6
	2013.45	3.1	0.34	0.34	0.32	2.2	142	...	...	6
	2013.96	3.8	0.41	0.39	0.20	2.2	170	...	...	6
	2014.45	2.5	0.34	0.31	0.35	2.1	108	...	...	6
	2015.04	2.9	0.35	0.31	0.34	2.2	146	...	...	6
	2015.29	1.6	0.59	0.24	0.17	1.9	141	...	...	6
	2015.33	1.3	0.58	0.26	0.16	1.8	123	...	...	6
	2015.35	1.6	0.58	0.24	0.18	1.9	123	...	...	6
	2015.38	2.4	0.45	0.28	0.27	2.1	124	...	...	6
	2016.21	3.2	0.49	0.27	0.24	2.2	166	...	...	7
	2016.44	2.1	0.29	0.33	0.38	2.1	97	...	...	7
	2016.47	3.0	0.44	0.25	0.31	2.2	124	...	...	7
	2016.54	2.7	0.42	0.29	0.29	2.1	160	...	...	7

References. (1) Boro Saikia et al. (2016); (2) Jeffers et al. (2014); (3) Jeffers et al. (2017); (4) Morgenthaler et al. (2012); (5) Fares et al. (2009); (6) Mengel et al. (2016); (7) Jeffers et al. (2018).

the existing literature (see Table 1), and show the available Ca II H&K indices in Figures 2–4. Although a correlation between mass-loss rate and Ca II H&K emission seems to exist for the Sun (visible in Figure 1), the correlation is complex; it is not obvious whether a similar relationship exists for other stars. If we were to use the correlation for the Sun to estimate the mass-loss rate variation of our sample stars, given their variability in Ca II H&K emission, i.e., $\Delta\dot{M} \propto \Delta S_{index}$, we would find a range of amplitudes around $\Delta\dot{M} = 0.01$–$1.5\langle\dot{M}\rangle$. Given the uncertainties, we simply adopt the same amplitude for the mass-loss rate as was determined for the Sun ($\Delta\dot{M} = 0.6\langle\dot{M}\rangle$), and require the function to reproduce the astropheric Lyα observations (i.e., $\dot{M}(t_{obs}) = \dot{M}_{obs}$). The solid black line in each figure represents this projected

variability. Note that, because the torque is a relatively weak function of mass-loss rate (see Equations (1)–(3)), our assumption about the amplitude of variability in mass-loss rate has a similarly weak effect on the amplitude of variability in the torque.

4. Angular Momentum-loss Rates

Here, we apply the FM18 braking law to our sample stars to calculate their stellar wind torques. We also calculate the rotational evolution torques from M15.

4.1. Predicted Alfvén Radii

Through the application of FM18 to our sample stars, we are able to examine their individual locations in our MHD
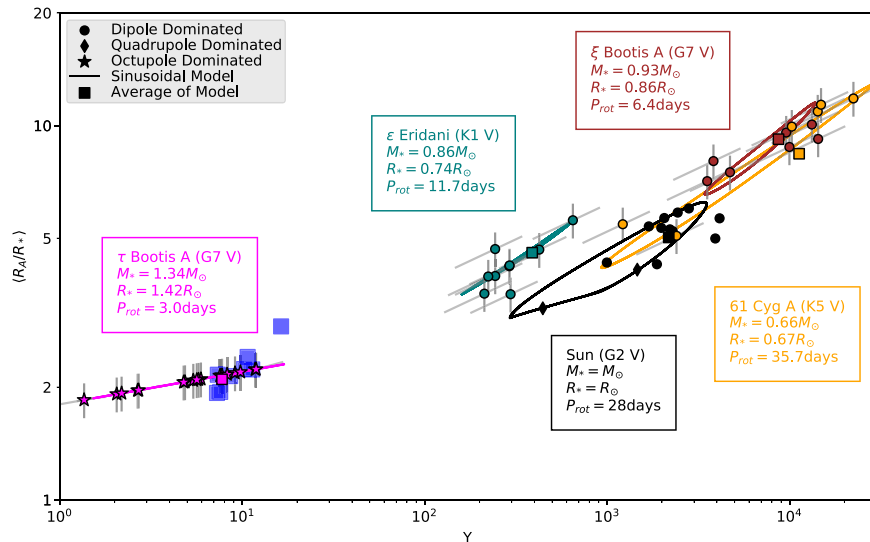
Figure 6. Average Alfvén radius vs. wind magnetization, Υ. Results for the Sun are shown in black. The ZDI epochs for 61 Cyg A (orange), ϵ Eri (teal), ξ Boo A (brown), and τ Boo A (magenta) are displayed with their uncertainties, in gray. The shape of each point signifies the magnetic geometry governing the angular momentum-loss rate according to Equation (3): dipolar-dominated with circles, quadrupolar-dominated with diamonds, and octupolar-dominated with stars. The sinusoidal models are shown with a corresponding colored line. Colored squares mark the average of both quantities for each star. The majority of ZDI epochs and solar magnetograms are dominated by the dipolar component—with the exception of τ Boo A, which hosts a weakly magnetized wind (according to the predictions of $\dot{M}$ of Nicholson et al. 2016) and so is dominated by the octupolar term in Equation (3). Results from the 3D MHD simulations of τ Boo A from Nicholson et al. (2016) are displayed using blue squares, in good agreement with this work.

parameter space. Figure 6 displays the location of each ZDI epoch and sinusoidal model in $\langle R_A \rangle - \Upsilon$ space. Uncertainties in the recovered field strengths from ZDI are difficult to quantify. Typically, errors quoted in ZDI papers are obtained by varying the input parameters to reconstruct additional ZDI maps, from which the variation in field strengths are quoted as error (see the discussion in Petit et al. (2008)). We propagate typical uncertainties for the magnetic field strength ($\pm 30\%$) and the mass-loss rates ($\pm 50\%$), respectively, using standard error analysis. The resulting uncertainty in wind magnetization, Υ, and the average Alfvén radius, $\langle R_A \rangle$, are correlated, as we show with diagonal gray lines in Figure 6. Vertical lines represent a $\pm 10\%$ uncertainty on our prediction of $\langle R_A \rangle$, which considers the approximations made in fitting Equation (3). This is discussed further in FM18 (see their Figure 10).

The wind magnetization parameterizes the effectiveness of the wind braking, or more physically, the size of the torque-averaged Alfvén radius. However, Equation (3) also encodes information about the magnetic geometry of the field, approximating this effect as a twice-broken power law. Depending on the strength of the three magnetic geometries considered here, the dipolar, quadrupolar, or octupolar (top, middle, or bottom) formula in Equation (3) will be used to calculate $\langle R_A \rangle$. To identify when each formula is used, different symbols are plotted in Figure 6.

The average Alfvén radii of our sample stars range from ~ 2 to $11 R_*$; most are typically dipole-dominated, with the exception of τ Boo A. The predicted $\langle R_A \rangle$ values for τ Boo A follow a shallower slope than the other dipolar-dominated stars, due to the weaker dependence of the octupolar geometry (as compared to the dipole or quadrupole geometries) on wind magnetization in Equation (3). The MHD model results of Nicholson et al. (2016) for the $\langle R_A \rangle$ of τ Boo A are also plotted with light blue squares in Figure 6. Their values for $\langle R_A \rangle$ are shown to be in good agreement with results from the FM18 braking law.

The Sun appears typical when compared with the three dipole-dominated stars; some have larger $\langle R_A \rangle$ and others have smaller. However, the Sun shows some quadrupolar-dominated behavior around solar maximum, which is not observed in the other dipole-dominated stars. Each sinusoidal model roughly represents the observed epochs from ZDI, and they are able to show how subsampling may skew our perception of where each star lies in this parameter space. A similar representation of the solar cycle in this parameter space was explored in the work of Pinto et al. (2011) (see Figure 11 within). We find (though we do not depict it here) that the sinusoidal prediction for the location of the Sun in this parameter space is representative of using the full data set examined in Paper I.

4.2. Torques

4.2.1. The Sun as a Star

In Paper I, we produced an estimate for the solar angular momentum-loss rate using the wealth of observations available for our closest star. Here, we instead treat the Sun as a star by reducing the number of observations to intervals of approximately 2 yr, thus illustrating the effect of sparse time sampling. Details on the selected magnetogram epochs are tabulated in Appendix A.

Figure 1 shows the result of our angular momentum-loss calculation. For the Sun, the dipole and octupole geometries are shown to cycle in phase, with the quadrupole out of phase, as previously discussed in DeRosa et al. (2012). The S-index values from Egeland et al. (2017) appear in phase with the quadrupolar geometry and the mass-loss rates taken from Paper I. The torques for each epoch using FM18 are plotted with black dots in the bottom panel. A gray line indicates the torque using the sinusoidal fits of the magnetic field and mass-loss rate.

From Figure 1, it is clear that simple sinusoids with fixed amplitude and phase are a poor fit to the data. This is primarily due to variation from cycle to cycle, i.e., the length of the Sun's magnetic cycle is know to vary, along with the strength of each

cycle (e.g., Solanki et al. 2002). However, the poor fit is also representative of the effects of sparse sampling on a system that contains variability on much shorter timescales than considered. Therefore, when considering the magnetic behavior of other stars, we expect not to see clear cyclical behaviors, even if the stars are truly cyclical, like we know the Sun to be.

We calculate the average torque for the solar magnetogram epochs to be 0.37×10^{30} erg, which is in close agreement with the estimate produced in Paper I. The sinusoidal fits produce an average torque of 0.30×10^{30} erg. The model torque has a different phase, with respect to the solar magnetic cycle, than using the full data set in Paper I, which is a consequence of fitting to sparsely sampled data. The torque given by M15 is 6.2×10^{30} erg. The discrepancy between these torques is discussed in Section 4.3.

4.2.2. 61 Cygni A

61 Cyg A was observed with ZDI by Boro Saikia et al. (2016) from 2007.59 to 2015.54, with an average of 1.19 yr between observations. They find the star to be very much like the Sun in its magnetic behavior: both the poloidal and toroidal field components reverse polarity in phase with its chromospheric activity, and it displays a weak, solar-like differential rotation profile. Like the Sun's, this global field is strongly dipolar: the dipole component strengthens at activity minimum, but weakens at activity maximum in favor of more multipolar field geometries.

Figures 2 and 6 display the full results of our angular momentum-loss calculation. Block dots in the bottom panel of Figure 2 plot the values of the torque calculated for the individual ZDI epochs using the projected mass-loss rates. The sinusoidal model torque is plotted with a solid gray line. The dipole component is strong, with activity minima in 2007 and 2014, so we predict a large average Alfvén radius ($\sim 10R_*$; see Figure 6). At the activity maximum around 2010, the field is at its most complex. However, the magnetic braking is still dominated by the dipolar component, due to the relative strengths of the other modes. This produces the smallest average Alfvén radius ($\sim 5R_*$).

The average torque for the ZDI epochs of 61 Cyg A, using FM18, is 0.20×10^{30} erg. The average of the sinusoidal model has a similar value of 0.18×10^{30} erg. The torque from M15 is calculated to be 5.25×10^{30} erg.

4.2.3. ε Eridani

ε Eri was observed with ZDI by Jeffers et al. (2014) from 2007.08 to 2014.98. Jeffers et al. (2014) originally monitored ε Eri with an average of 1.11 yr between observations until 2013.75. Jeffers et al. (2017) followed up these observations taking three observations in quick succession (approximately once a month) during its activity minimum. The magnetic geometry of ε Eri at minimum activity is more complicated than the axisymmetric dipolar structure seen from the Sun and 61 Cyg A. The dipole component instead strengthens at activity maxima, producing the largest Alfvén radii when the chromospheric activity is highest. Figure 3 details the angular momentum-loss calculation for ε Eri, and the average Alfvén radii are displayed in Figure 6.

The ZDI epochs of ε Eri, using FM18, have an average torque of 1.00×10^{31} erg. With the sinusoidal fits, we find a larger average value of 1.24×10^{31} erg. The sinusoidal model suggests that the ZDI epochs have preferentially sampled

minima of activity, and therefore average to a lower torque. We calculate the torque using M15 and find a value of 1.14×10^{32} erg.

4.2.4. ξ Bootis A

The magnetic variability of ξ Boo A is unlike both 61 Cyg A and ε Eri. It was observed with ZDI by Morgenthaler et al. (2012) from 2007.59 to 2011.07, with an average time between observations of half a year. The star hosts a persistent toroidal component with fixed polarity through all observations. This field contains a large fraction of the magnetic energy, shown by the mean field strength (gray dots) in the top panel of Figure 4 being much larger than the combined magnetic field strength (black dots). The total magnetic field appears to have short time variability. However, the second panel in Figure 4 appears to show a coherent pattern. With the limited data available, and no cyclic variability detected in other activity indicators, we fit a sinusoid to this slowly varying magnetic geometry.

Note that the data are best-represented with maxima occurring where there are no data. The existence and amplitude of the fit maxima are poorly constrained by the available data, and the sinusoidal fit is merely speculative. This leads the torque for the cycle, shown with a solid gray line in the bottom panel of Figure 4, to be much larger than the ZDI epochs, shown with black dots.

The average torque calculated for the ZDI epochs of ξ Boo A, using FM18, is 2.31×10^{31} erg. Averaging the sinusoidal model instead, we produce a torque of 3.10×10^{31} erg. The rotational evolution torque from M15 gives a value of 7.48×10^{32} erg.

4.2.5. τ Bootis A

τ Boo A is currently the star most extensively monitored with ZDI (Donati et al. 2008; Fares et al. 2009; Mengel et al. 2016; Jeffers et al. 2018). From these studies, authors have found τ Boo A to have a magnetic cycle with polarity reversals in phase with its chromospheric activity cycle of 120 day, as observed for the Sun and 61 Cyg A. Its mass-loss rate is not observationally constrained, but MHD simulations of the stellar wind surrounding τ Boo A have been produced by Nicholson et al. (2016), using maps from some of the ZDI epochs considered here. We include these results in Figure 5, using blue squares to indicate their derived mass-loss rates and angular momentum-loss rates. We calculate the torque-averaged Alfvén radii associated with these simulated values using Equation (1), and display them in Figure 6 as light blue squares. For clarity, we also show a phase-folded version of Figure 5 in Appendix B (Figure 8).

Equation (3) predicts the efficiency of angular momentum loss to be low and dominated by the octupolar scaling. Both this work and the simulations of Nicholson et al. (2016) predict a torque-averaged lever arm of $\sim 2R_*$, which is much lower than the other stars in the sample (see Figure 6). We calculate the average torque from the ZDI epochs of τ Boo A, using FM18, to be 1.23×10^{32} erg. The sinusoidal model has an average torque of 1.32×10^{32} erg. The torque from M15 is calculated to be 3.67×10^{32} erg.

4.3. Comparison of Torques

In Figure 7, the predictions of M15 for each star are shown with a range of Rossby numbers, using solid lines. We indicate the torque for each star in this model, at its respective Rossby
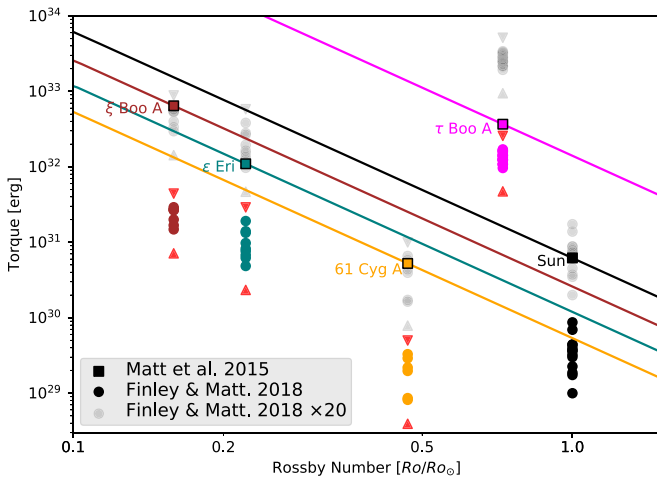
Figure 7. Angular momentum-loss rate vs. Rossby number. Solid lines represent the M15 models for each star in our sample, over a range of Rossby numbers. Colored squares indicate the predicted value, given our calculated Rossby numbers in Table 1. The torques computed from ZDI epochs and the FM18 braking law are shown with colored circles. The range of observational uncertainty in the prediction of FM18 is shown with red limiting triangles. In all cases, the modeled torques using FM18 are lower when compared to those from M15. Multiplication of the FM18 torques by a factor of 20, shown in gray, brings the models toward rough agreement.

number from Table 1, with a colored square. The torques using FM18 and the multiple ZDI epochs are shown with corresponding colored circles. As with Figure 6, typical uncertainties in observed rotation rates ($\pm 10\%$), mass-loss rates ($\pm 10\%$), and field strengths (± 1G) of each star lead to errors in the predictions of Equations (1)–(3). The range of possible torques for each star, given these uncertainties, is indicated with red limits. While these uncertainties are significant, they are not large enough to affect any of our conclusions. For the dipole-dominated stars, the FM18 torques appear systematically lower than those expected from M15, by a factor of roughly 10–30. Gray points show the result of multiplying all the FM18 torques by a factor of 20, which brings all of the dipole-dominated stars into agreement.

However, τ Boo A requires a much smaller factor of ~ 3 to bring the two torques into agreement. Why the torques for τ Boo A are in better agreement than the other stars' is unknown. However, it is worth noting that the mass-loss rate for this star has not been measured. Instead, we used the average mass-loss rate from Nicholson et al. (2016), which is directly dependent on their choice of base wind density and temperature. Given that these quantities are not constrained well by observations, the mass-loss rates obtained from these simulations are effectively (although indirectly) assumed a priori. The same is true for all such models. If the true mass-loss rate is smaller than the value used here, the difference between torques may increase such that we may find a truly systematic value between the two methods for all of the sample stars. If the mass-loss rate of τ Boo A were smaller, its torque might also become dipole-dominated like the rest of the sample.

5. Discussion

5.1. Systematic Differences between the FM18 and M15 Torques

For all the stars in our sample, the torques from FM18 systematically predict lower angular momentum-loss rates when

compared to the rotational evolution torques from M15. This was also the case in Paper I, wherein we suggested a possible solution: the Sun may be in a low torque state at present. Given that all five stars here are low, and it seems unlikely that they would all be in a low state, a different explanation should be explored.

A systematic difference between the FM18 and M15 torques suggests there should be sources of underestimation in either the MHD modeling, the rotation-evolution models, or the observed properties of these stars. Paper I showed that, for the Sun, using the surface field strength leads to a torque estimate lower than those based on the open magnetic flux, by a factor of ~ 7. It remains unclear why this is so. It may be due to underestimation of field strengths in magnetograms, or to the coronal magnetic field becoming open much closer to the solar surface. Underprediction of the open magnetic flux will artificially reduce the braking torque, given the strong correlation shown by Réville et al. (2015).

There are likely also systematics in the magnetic field strengths obtained from ZDI. It is well-known that ZDI does not reconstruct all of the photospheric magnetic field due to flux cancellation effects (Reiners & Basri 2009; Lehmann et al. 2018; V. See et al. 2019a, in preparation). Recently, Lehmann et al. (2019) showed that ZDI sometimes underestimates the field strengths of the large-scale field components, i.e., the dipole, quadrupole, and octupole, by a factor of a few. Consequently, the spin-down torques will also be underestimated (see also the discussion by V. See et al. (2019b), in preparation). Additionally, the method used to calculate $\mathcal{R}_{\mathrm{dip}}$, $\mathcal{R}_{\mathrm{quad}}$, and $\mathcal{R}_{\mathrm{oct}}$ from the results of ZDI may lead to underestimation of the strength of the magnetic field. Given the inherent non-axisymmetry of the ZDI fields, the values we calculate simply approximate the relative strengths of each component. Typically, the polar field values required for the Equation (3) will be larger than the global average field strength used in this work, but the effect this has is not large enough to modify our conclusions.

To increase the FM18 torques by a factor of 20, for example, would require $\sim 4\times$ greater average Alfvén radii (or $\sim 26\times$ stronger dipole field strengths) than observed. Based on this, it is not clear whether this discrepancy can be explained with our current knowledge. Perhaps a combination of wind energetics (as discussed in Paper I for the open flux problem) and the systematics of ZDI might be able to explain the underprediction of the FM18 torques versus those of M15.

5.2. The Impact of Magnetic Variability on Dynamical Torque Estimates

During each sequence of ZDI observations, our sample stars experience variability in their global magnetic field strength and topology. In Figure 6, the predicted average Alfvén radii for each ZDI epoch are plotted with a symbol that represents the governing topology in Equation (3). In the majority of cases, despite strengthening of the multipolar components, the dipole component governs the location of the torque-averaged Alfvén radius.

Similarly, V. See et al. (2019b, in preparation) show, for a large range of stars observed with ZDI, that Equation (3) predicts angular momentum-loss rates to be dominated by the dipolar component. However, for sufficiently high mass-loss rates and weak dipolar fields, as seen in this work with τ Boo A, some stars can have multipolar-dominated wind braking. These stars possess low wind magnetizations and therefore have small average Alfvén radii. Note that, if the field strengths are underestimated, as discussed in Section 5.1, even τ Boo A could then be dipole-dominated.

In general, the extrema of the torques from our ZDI stars are 0.5–1.9 times the average torque, $\langle\tau_{\rm FM18}\rangle$. Using the subsampled solar epochs, we find the maximum torque to be $2.3\langle\tau_{\rm FM18}\rangle$. If we instead consider the complete data set from Paper I, we find the maximum torque to be $2.5\langle\tau_{\rm FM18}\rangle$, slightly larger than the subsampled value. Similarly, for other stars, we expect that the true amplitude of variability could be larger than represented by the sparse sampling. The next-largest amplitude of variation is found for ϵ Eri, where the maximum torque is $1.9\langle\tau_{\rm FM18}\rangle$ in the ZDI epoch of 2013.75. The smallest amplitude of torque variability belongs to τ Boo A, which has a minimum torque of $0.7\langle\tau_{\rm FM18}\rangle$, and a maximum torque of $1.3\langle\tau_{\rm FM18}\rangle$.

We find results gained by subsampling the solar data set produce average torques that are dependent on the selected magnetogram epochs. For example, by changing the length of the available data set and selecting a different set of 13 epochs, we can find average torques of 0.3–0.4×10^{30} erg, due to preferentially selecting epochs from cycle 24 or 23, respectively (with 23 being stronger than 24). Equally, reducing the number of epochs used in the data set from 13 to 6 can change the average torque to a similar degree, but also generally decreases the maximum torque to values comparable to those of the ZDI stars ($\sim 2\langle\tau_{\rm FM18}\rangle$). Reducing the number of epochs further can lead to extreme values in the average torques from 0.1 to 0.8×10^{30} erg, due to short-term variability in the data set.

Estimates like this for the Sun hint at how a restricted data set may bias the time-varying torque estimates for other stars. Based on the results from this work, it appears that stellar wind variability has a much smaller effect than is required to remedy the discrepancy between stellar wind torques and their long-time rotation evolution counterparts. However, variability can confuse the issue and should be accounted for in future works.

5.3. Establishing the Timescales of Variability

In this work, we are able to calculate the time-varying torque for four stars with a cadence of $\sim$1–2 yr, over a period of nearly decade. The torque's variation due to magnetic variability can be thought of as an uncertainty in estimating the current average torque for a given star based on a single observation. In Paper I, the variability of the solar wind was examined on a much shorter ($\sim$27 day) cadence over two decades, so we were able to estimate the torque more continuously. Even so, variability in the solar wind is observed on still-shorter timescales. These day-to-day and hour-to-hour variations in the solar wind are averaged in our calculations in Paper I, in order to better represent the global wind when using observations from a single in situ location. The impact such fluctuations have on the 27 day torque averages remains an open question.

On timescales of centuries to millennia (still shorter than the braking timescale), there is also evidence for further magnetic variability. For the Sun, indirect methods of detecting this variability, such as examining the concentration of cosmogenic radionuclides (^{14}C, ^{10}Be, etc.) in tree trunks or polar ice cores, have been successful at recovering changes in the magnetic field over the last millennium (Wu et al. 2018). For other stars, we are unable to examine the evolution of their magnetism for longer than current observations allow. However, the observed spread of magnetic activity indicators (e.g., X-rays;

Wright et al. 2011) around their secular trends could be caused by variability (as opposed to true differences in stars' average properties). It is still not clear how such long-term variability may skew our current evaluation of stellar braking torques.

6. Conclusion

In this paper, we have quantified the effect of observed magnetic variability on the predicted angular momentum-loss rates for four Sun-like stars. Our sample stars have all been repeatedly observed with ZDI, which provides information on the topology of the magnetic field. This information is then combined with estimates of their mass-loss rates from studies of astrospheric Lyα, as well as a relationship for the stellar wind braking given by FM18. We compare these time-varying estimates of the angular momentum-loss rate to the long-time-averaged value predicted by M15, a rotational evolution model.

We find that, similarly to what was found for the Sun in Paper I, the angular momentum-loss rates predicted vary significantly (roughly 0.5–1.5 times their average values), such that torques calculated using single observational epochs can differ from the decadal average torque on the star. This represents an uncertainty when calculating torques for stars with single epochs of observation.

Our calculated angular momentum-loss rates based on FM18 are found to be systematically lower than the long-time-averaged torques required by M15. We do not know the origin of this discrepancy, but it could be due (at least in part) to several factors: the open flux problem, whereby wind models currently underpredict the observed open magnetic flux for the Sun; problems with observed parameters, such as the potential systematic effects from the ZDI technique in recovering the correct field strengths (Lehmann et al. 2019); problems with rotation-evolution models; or longer-term variability in the torque. Such longer-term variability has the potential to affect our predictions for the long-time ($\sim$10–100 Myr) average torque required by rotation evolution models.

Appendix A
Sun-as-a-star Data

Table 3 displays the selected magnetogram observations from *SOHO*/MDI and *SDO*/HMI used in Figure 1, along with the results of the angular momentum-loss calculation using

Table 3
Solar Magnetic Properties and Angular Momentum-loss Results

Star Name	Magnetogram Epoch (Instrument)	B_* (G)	$\mathcal{R}_{dip}$ $\equiv B_{dip}/B_*$	$\mathcal{R}_{quad}$ $\equiv B_{quad}/B_*$	$\mathcal{R}_{oct}$ $\equiv B_{oct}/B_*$	$\langle R_A \rangle / R_*$	τ_{FM18} $(\times 10^{30}$ erg$)$	τ_{M15} $(\times 10^{30}$ erg$)$	$\frac{\tau_{M15}}{\langle \tau_{FM18} \rangle}$
Sun	1996.76(MDI)	8.0	0.38	0.11	0.51	5.9	0.87	6.20	16.55
	1998.49(MDI)	7.5	0.37	0.18	0.45	6.0	0.69	⋯	⋯
	2000.65(MDI)	5.7	0.22	0.16	0.62	4.3	0.30	⋯	⋯
	2002.37(MDI)	8.1	0.21	0.32	0.47	5.0	0.39	⋯	⋯
	2004.16(MDI)	6.6	0.27	0.06	0.67	5.7	0.32	⋯	⋯
	2005.88(MDI)	6.1	0.32	0.15	0.53	5.3	0.44	⋯	
	2007.59(MDI)	5.2	0.34	0.09	0.57	5.3	0.37	⋯	⋯
	2009.31(MDI)	3.9	0.38	0.06	0.56	5.7	0.23	⋯	⋯
	2011.18(HMI)	3.1	0.30	0.33	0.37	4.3	0.17	⋯	⋯
	2012.89(HMI)	2.1	0.23	0.30	0.47	3.2	0.10	⋯	⋯
	2014.61(HMI)	4.1	0.21	0.50	0.29	4.1	0.19	⋯	⋯
	2016.33(HMI)	5.7	0.31	0.29	0.40	5.2	0.36	⋯	⋯
	2018.12(HMI)	5.2	0.38	0.07	0.55	5.4	0.44	⋯	⋯

both the formulae from FM18 and M15, where symbols have the same meaning as in Table 2.

Appendix B
Alternative View of τ Bootis A Data

Here, we show the result of phase-folding the data from Figure 5 (Figure 8). τ Boo A is estimated to have a short magnetic cycle period of around 240 days, which is in-phase with its 120 day chromospheric activity cycle. We phase-fold the data for τ Boo A on the timescale of its chromospheric cycle, rather than its magnetic cycle, as our predictions do not consider the polarity of the magnetic field. Given cycle-to-cycle variation in length and strength, fitting a simple sinusoid does not fit all of the magnetic variation well.
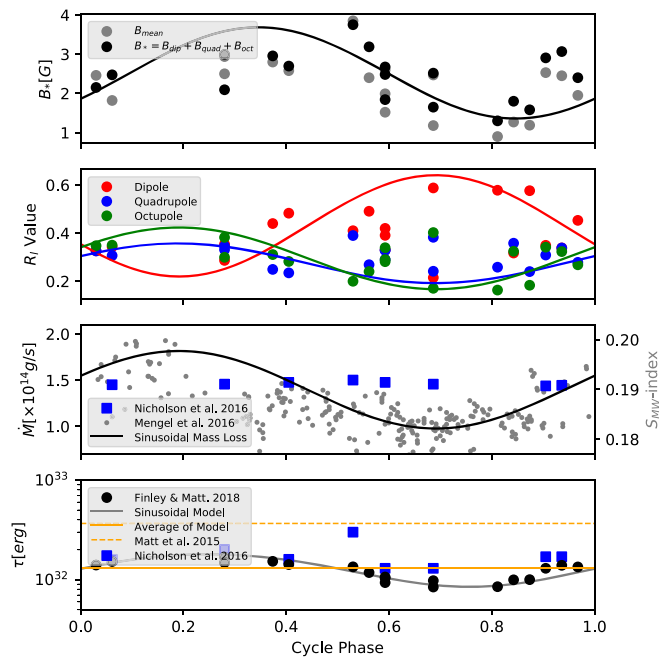
Figure 8. Same as Figure 5, with the data phase folded into the 120 day chromospheric cycle.

ORCID iDs

Adam J. Finley ⓘ https://orcid.org/0000-0002-3020-9409
Sean P. Matt ⓘ https://orcid.org/0000-0001-9590-2274

References

Amard, L., Palacios, A., Charbonnel, C., Gallet, F., & Bouvier, J. 2016, A&A, 587, A105
Babcock, H. 1961, ApJ, 133, 572
Babcock, H. D. 1959, ApJ, 130, 364
Baines, E. K., & Armstrong, J. T. 2011, ApJ, 744, 138
Baliunas, S., Donahue, R., Soon, W., et al. 1995, ApJ, 438, 269
Barnes, S. A. 2003, ApJ, 586, 464
Barnes, S. A. 2007, ApJ, 669, 1167
Barnes, S. A. 2010, ApJ, 722, 222
Barnes, S. A., & Kim, Y.-C. 2010, ApJ, 721, 675
Boeche, C., & Grebel, E. 2016, A&A, 587, A2
Boro Saikia, S., Jeffers, S., Morin, J., et al. 2016, A&A, 594, A29
Boro Saikia, S., Lueftinger, T., Jeffers, S., et al. 2018, A&A, 620, L11
Borsa, F., Scandariato, G., Rainer, M., et al. 2015, A&A, 578, A64
Bouvier, J., Matt, S. P., Mohanty, S., et al. 2014, in Protostars and Planets VI, ed. H. Beuther et al. (Tucson, AZ: Univ. Arizona Press), 433
Boyajian, T. S., von Braun, K., van Belle, G., et al. 2013, ApJ, 771, 40
Brown, A. G., Vallenari, A., Prusti, T., et al. 2016, A&A, 595, A2
Brown, S., Donati, J.-F., Rees, D., & Semel, M. 1991, A&A, 250, 463
Brun, A., Browning, M., Dikpati, M., Hotta, H., & Strugarek, A. 2015, SSRv, 196, 101
Brun, A. S., & Browning, M. K. 2017, LRSP, 14, 4
Caligari, P., Moreno-Insertis, F., & Schussler, M. 1995, ApJ, 441, 886
Cranmer, S. R., & Saar, S. H. 2011, ApJ, 741, 54
Delorme, P., Cameron, A. C., Hebb, L., et al. 2011, MNRAS, 413, 2218
DeRosa, M., Brun, A., & Hoeksema, J. 2012, ApJ, 757, 96
Donahue, R. A., Saar, S. H., & Baliunas, S. L. 1996, ApJ, 466, 384
Donati, J.-F., & Brown, S. 1997, A&A, 326, 1135
Donati, J.-F., & Landstreet, J. 2009, ARA&A, 47, 333
Donati, J.-F., Moutou, C., Fares, R., et al. 2008, MNRAS, 385, 1179
Donati, J.-F., Semel, M., Carter, B. D., Rees, D., & Cameron, A. C. 1997, MNRAS, 291, 658
Donati, J.-F., Semel, M., & Praderie, F. 1989, A&A, 225, 467
Eberhard, G., & Schwarzschild, K. 1913, ApJ, 38, 292
Egeland, R., Soon, W., Baliunas, S., et al. 2017, ApJ, 835, 25

Fan, Y. 2008, ApJ, 676, 680
Fares, R., Donati, J.-F., Moutou, C., et al. 2009, MNRAS, 398, 1383
Finley, A. J., & Matt, S. P. 2017, ApJ, 845, 46
Finley, A. J., & Matt, S. P. 2018, ApJ, 854, 78
Finley, A. J., Matt, S. P., & See, V. 2018, ApJ, 864, 125
Fisher, G., Fan, Y., Longcope, D., Linton, M., & Pevtsov, A. 2000, SoPh, 192, 119
Fuhrmann, K. 2004, AN, 325, 3
Gallet, F., & Bouvier, J. 2013, A&A, 556, A36
Gallet, F., & Bouvier, J. 2015, A&A, 577, A98
Garraffo, C., Drake, J. J., & Cohen, O. 2016, A&A, 595, A110
Gilliland, R. 1986, ApJ, 300, 339
Gray, D. F., Baliunas, S. L., Lockwood, G., & Skiff, B. A. 1996, ApJ, 465, 945
Gunn, A., Mitrou, C., & Doyle, J. 1998, MNRAS, 296, 150
Hall, J. C., Lockwood, G., & Skiff, B. A. 2007, AJ, 133, 862
Hartmann, L., Schmidtke, P., Davis, R., et al. 1979, ApJL, 233, L69
Hartmann, L. W., & Noyes, R. W. 1987, ARA&A, 25, 271
Hick, P., & Jackson, B. 1994, AdSpR, 14, 135
Hunter, J. D. 2007, CSE, 9, 90
Janson, M., Reffert, S., Brandner, W., et al. 2008, A&A, 488, 771
Jardine, M., Vidotto, A., van Ballegooijen, A., et al. 2013, MNRAS, 431, 528
Jeffers, S., Boro Saikia, S., Barnes, J., et al. 2017, MNRAS, 471, L96
Jeffers, S., Mengel, M., Moutou, C., et al. 2018, MNRAS, 479, 5266
Jeffers, S., Petit, P., Marsden, S., et al. 2014, A&A, 569, A79
Keppens, R., & Goedbloed, J. 1999, A&A, 343, 251
Kervella, P., Mérand, A., Pichon, B., et al. 2008, A&A, 488, 667
Landin, N., Mendes, L., & Vaz, L. 2010, A&A, 510, A46
Lean, J., Cook, J., Marquette, W., & Johannesson, A. 1998, ApJ, 492, 390
Lehmann, L. T., Hussain, G. A. J., Jardine, M. M., Mackay, D. H., & Vidotto, A. A. 2019, MNRAS, 483, 5246
Lehmann, L. T., Jardine, M. M., Mackay, D. H., & Vidotto, A. A. 2018, MNRAS, 478, 4390
Mamajek, E. E., & Hillenbrand, L. A. 2008, ApJ, 687, 1264
Marsden, S., Petit, P., Jeffers, S., et al. 2014, MNRAS, 444, 3517
Matt, S., & Pudritz, R. E. 2008, ApJ, 678, 1109
Matt, S. P., Brun, A. S., Baraffe, I., Bouvier, J., & Chabrier, G. 2015, ApJL, 799, L23
Matt, S. P., MacGregor, K. B., Pinsonneault, M. H., & Greene, T. P. 2012, ApJL, 754, L26
McComas, D., Angold, N., Elliott, H., et al. 2013, ApJ, 779, 2
McComas, D., Barraclough, B., Funsten, H., et al. 2000, JGRA, 105, 10419
McComas, D., Elliott, H., Schwadron, N., et al. 2003, GeoRL, 30, 1517
Meibom, S., Barnes, S. A., Platais, I., et al. 2015, Natur, 517, 589
Meibom, S., Mathieu, R. D., & Stassun, K. G. 2009, ApJ, 695, 679
Mengel, M., Fares, R., Marsden, S., et al. 2016, MNRAS, 459, 4325
Mestel, L. 1968, MNRAS, 138, 359
Metcalfe, T., Buccino, A. P., Brown, B., et al. 2013, ApJL, 763, L26
Mittag, M., Robrade, J., Schmitt, J., et al. 2017, A&A, 600, A119
Morgenthaler, A., Petit, P., Saar, S., et al. 2012, A&A, 540, A138
Neugebauer, M., Liewer, P., Smith, E., Skoug, R., & Zurbuchen, T. 2002, JGRA, 107, 1488
Nicholson, B., Vidotto, A., Mengel, M., et al. 2016, MNRAS, 459, 1907
Noyes, R., Hartmann, L., Baliunas, S., Duncan, D., & Vaughan, A. 1984, ApJ, 279, 763
Ossendrijver, M. 2003, A&ARv, 11, 287
Owens, M. J., Crooker, N., & Lockwood, M. 2011, JGRA, 116, A04111
Pantolmos, G., & Matt, S. P. 2017, ApJ, 849, 83
Parker, E. N. 1955, ApJ, 121, 491
Parker, E. N. 1958, ApJ, 128, 664
Petit, P., Dintrans, B., Morgenthaler, A., et al. 2009, A&A, 508, L9
Petit, P., Dintrans, B., Solanki, S., et al. 2008, MNRAS, 388, 80
Pinto, R. F., Brun, A. S., Jouve, L., & Grappin, R. 2011, ApJ, 737, 72
Pizzolato, N., Maggio, A., Micela, G., Sciortino, S., & Ventura, P. 2003, A&A, 397, 147
Pneuman, G., & Kopp, R. A. 1971, SoPh, 18, 258
Ramesh, K. 2010, ApJL, 712, L77
Reiners, A., & Basri, G. 2009, A&A, 496, 787
Réville, V., Brun, A. S., Matt, S. P., Strugarek, A., & Pinto, R. F. 2015, ApJ, 798, 116
Réville, V., Folsom, C. P., Strugarek, A., & Brun, A. S. 2016, ApJ, 832, 145
Robrade, J., Schmitt, J., & Favata, F. 2012, A&A, 543, A84
Rüedi, I., Solanki, S., Mathys, G., & Saar, S. 1997, A&A, 318, 429
Schrijver, C., Cote, J., Zwaan, C., & Saar, S. 1989, ApJ, 337, 964
Schrijver, C. J., & Liu, Y. 2008, SoPh, 252, 19
Schwenn, R. 2006, SSRv, 124, 51
See, V., Jardine, M., Vidotto, A., et al. 2016, MNRAS, 462, 4442

Semel, M. 1989, A&A, 225, 456
Skumanich, A. 1972, ApJ, 171, 565
Solanki, S., Krivova, N., Schüssler, M., & Fligge, M. 2002, A&A, 396, 1029
Song, I., Caillault, J.-P., y Navascués, D. B., Stauffer, J. R., & Randich, S. 2000, ApJL, 533, L41
Spruit, H. C. 1981, A&A, 98, 155
Stelzer, B., & Neuhäuser, R. 2001, A&A, 377, 538
Sun, X., Hoeksema, J. T., Liu, Y., & Zhao, J. 2015, ApJ, 798, 114
Takeda, G., Ford, E. B., Sills, A., et al. 2007, ApJS, 168, 297
Testa, P., Saar, S. H., & Drake, J. J. 2015, RSPTA, 373, 20140259
Toner, C., & Gray, D. F. 1988, ApJ, 334, 1008
Van Saders, J. L., & Pinsonneault, M. H. 2013, ApJ, 776, 67
Vidotto, A., Gregory, S., Jardine, M., et al. 2014, MNRAS, 441, 2361
Walker, G. A., Croll, B., Matthews, J. M., et al. 2008, A&A, 482, 691
Wang, Y.-M., Lean, J., & Sheeley, N. 2000, GeoRL, 27, 505

Wang, Y.-M., & Sheeley, N. 1990, ApJ, 355, 726
Webb, D. F., & Howard, R. A. 1994, JGRA, 99, 4201
Webb, D. F., & Howard, T. A. 2012, LRSP, 9, 3
Weber, E. J., & Davis, L. 1967, ApJ, 148, 217
Wenzler, T., Solanki, S., Krivova, N., & Fröhlich, C. 2006, A&A, 460, 583
Wilson, O. 1978, ApJ, 226, 379
Wolff, S., & Simon, T. 1997, PASP, 109, 759
Wood, B. E. 2004, LRSP, 1, 1
Wood, B. E., & Linsky, J. L. 1998, ApJ, 492, 788
Wood, B. E., Müller, H.-R., Zank, G. P., & Linsky, J. L. 2002, ApJ, 574, 412
Wood, B. E., Müller, H.-R., Zank, G. P., Linsky, J. L., & Redfield, S. 2005, ApJL, 628, L143
Wright, N. J., Drake, J. J., Mamajek, E. E., & Henry, G. W. 2011, ApJ, 743, 48
Wu, C. J., Usoskin, I., Krivova, N., et al. 2018, A&A, 615, A93
Zeeman, P. 1897, Natur, 55, 347